Pergamon

PII: S0191-8141(97)00006-0

Journal of Structural Geology, Vol. 19, No. 5, pp. 603 to 620, 1997

0191-8141/97 $17.00 + 0.00

Fracturing of garnet crystals in anisotropic metamorphic rocks during uplift

SHAOCHENG JI, PINGLAO ZHAO and KAZUKO SARUWATARI

Département de géologie, Université de Montréal, C.P. 6128, Succursale 'Centre-Ville', Montréal, Québec, Canada H3C 3J7

(*Received* 27 *March* 1996; *accepted in revised form* 6 *January* 1997)

Abstract—Garnet crystals in granulite-facies mylonites and gneisses from the Morin shear zone in the Grenville Province (Québec) are characterized by pervasive, closely spaced, relatively straight, tensile fractures aligned systematically normal to the mylonitic foliation and lineation. The fractures developed preferentially in coarse grains (> 0.2 mm) or in grains with a large aspect ratio (> 2). Fractured segments of each garnet crystal have not been separated or filled with matrix minerals (quartz and feldspar) or with retrograde minerals (biotite, muscovite and chlorite). This suggests that the garnets were fractured at shallow crustal depths ($T < 300°C$ or < 15 km for a thermal gradient 20°C/km). We propose that the garnet fractures were formed by the response of anisotropic metamorphic rocks to a horizontal extension during uplift and cooling of the metamorphic terrane within the upper crust. Using a modified shear-lag theory, we can explain why tensile fracturing took place preferentially in stiff garnet rather than in felsic material, and why the fractures are unequally spaced in a garnet grain. Our data suggest that the sequential tensile fractures of garnet grains record a progressive uplift process of metamorphic rocks within the upper crust. © 1997 Elsevier Science Ltd.

INTRODUCTION

Pervasive, closely spaced, foliation-perpendicular, brittle extension fractures of garnet crystals are very common in high-grade, foliated and lineated metamorphic rocks (e.g. Martignole, 1975; Petrakakis, 1986; Ji *et al.*, 1993; Prior, 1993; Elvevold *et al.*, 1994; Ji and Martignole, 1994; Moecher and Wintsch, 1994; Indares, 1995; Whitney, 1996). The garnet fractures may be observed both in the field and under the microscope. However, to our knowledge, they have not been studied explicitly and in detail in the literature. In this paper, we choose high-grade mylonites and gneisses from the Morin shear zone (MSZ) of Grenville Province (Québec) as an example to demonstrate characteristics of garnet fractures and to analyze the origin of the fractures.

GEOLOGICAL SETTING

The MSZ constitutes the eastern limit of the Morin terrane which belongs to the southern part of the Canadian Grenville Province (Rivers *et al.*, 1989) (Fig. 1). The central part of this terrane is occupied by the Morin anorthosite which consists of a dome emplaced as a diapir during the Grenville orogenic cycle (1154 Ma, U/Pb on zircon; Doig, 1991) and an eastern lobe that was considered to be a nappe thrust towards the east (Martignole and Schrijver, 1970) but is now interpreted as a portion of the MSZ (Martignole *et al.*, 1995). The MSZ consists of highly strained, metasedimentary and metaplutonic rocks with a well-developed, W-dipping mylonitic foliation and a prominently subhorizontal stretching lineation. Outcrop-scale isoclinal folds have their axes parallel to the stretching lineation (Fig. 2a). Mineral assemblages of these rocks were equilibrated at granulite-facies conditions and have suffered very little retrometamorphism, indicating rapid uplift and cooling of these rocks and lack of water inflow. Kinematic indicators such as winged porphyroclasts, *C–S* structures, asymmetric boudins and extensional shear bands indicate that the MSZ was dextral transcurrent and that it represents a lateral ramp along which the Morin terrane was displaced towards the north during the period between 1155 and 1030 Ma (Martignole *et al.*, 1995). The high-grade metamorphic rocks of the MSZ had been uplifted to the Earth's surface before 544 Ma ago as they are covered by Cambrian and Ordovician horizontal strata.

The garnet-bearing metamorphic rocks in the MSZ are mainly pelitic, charnockitic, quartzitic, granitic and mafic mylonites, and gneisses. Strong ribbon and streaky shape-preferred orientation are manifested by these rocks. The quartzitic and granitic mylonites are characterized by highly strained quartz grains with scalloped or amoeboid grain boundaries preserving evidence of grain-boundary migration. The charnockitic gneisses are characterized by an annealed microstructure of quartz including strain-free polygonal grains with straight grain boundaries. Garnet represents about 2–7 vol. % of the quartzitic, granitic and charnockitic mylonites and gneisses, and 10–20 vol. % of the pelitic and mafic gneisses. Outcrop-scale mode I joints (Price and Cosgrove, 1990) are preferentially oriented subnormal to the subhorizontal mylonitic lineation (Fig. 2).

CHARACTERISTICS OF FRACTURED GARNET

Garnet is commonly isolated in a ductilely deformed matrix of feldspars and particularly quartz (Figs 3 & 4). Electron microprobe data show that the garnets have

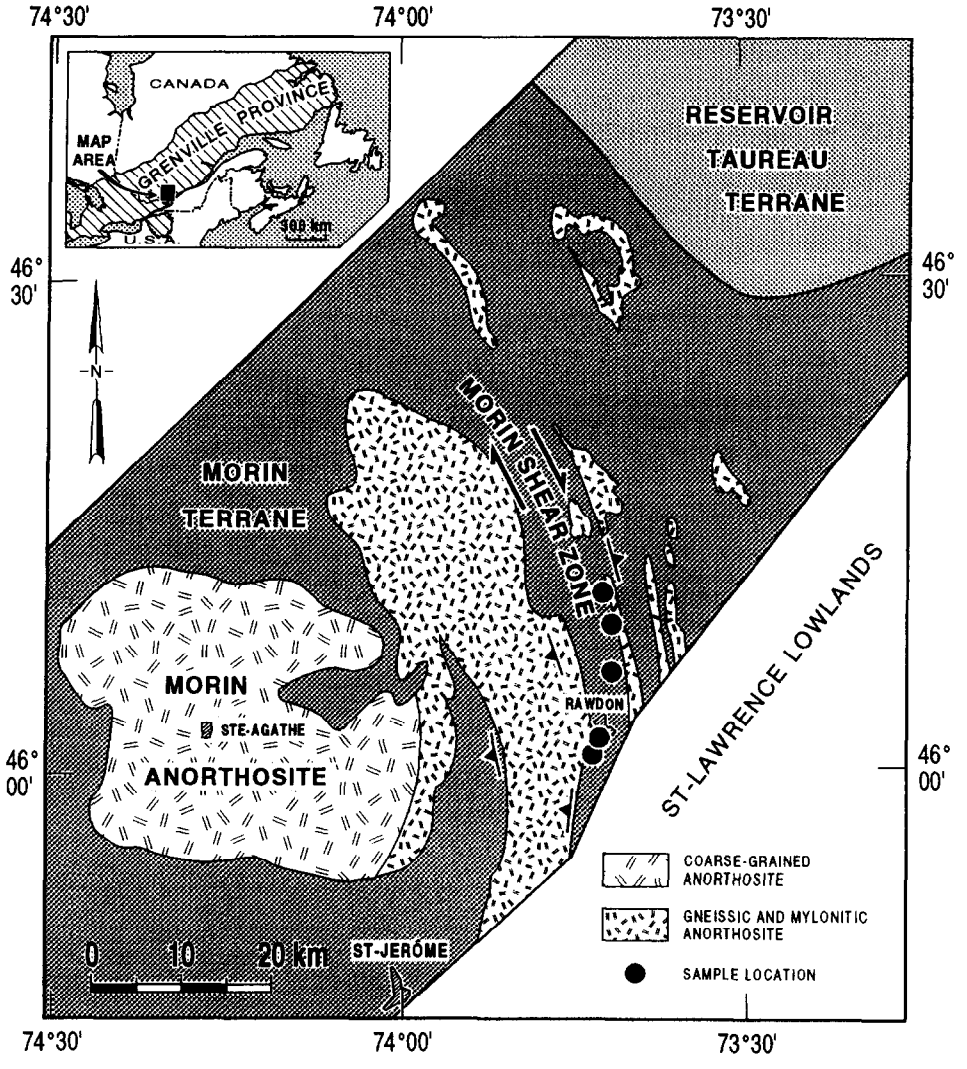

Fig. 1. Geological map showing the location of the Morin shear zone and those of the studied samples. The inset map shows the Grenville Province in Canada.

almost identical composition (almandine 61–65%, pyrope 20–30%, grossular 3–10%, spessartine 1–5%) and there is no significant compositional variation from core to rim. The garnet composition close to a fracture wall is the same as the bulk of the garnet crystal. The absence of compositional variation in the garnets can be attributed to homogenization by effective diffusion at high temperature (Yardley, 1977), to the absence of exchange reactions between garnet and adjacent minerals (quartz and feldspar) during cooling (Ji and Martignole, 1994) and to the low-temperature environment during the fracturing of garnets.

Large thin sections (7 × 5 cm) parallel to the mylonitic lineation and perpendicular to the foliation were used for statistical characterization of microfractures in garnet grains. Under the optical microscope, the following parameters were measured for all the garnet grains in each thin section (Fig. 5): (1) the maximum length ($2L$); (2) the maximum width ($2r_0$); (3) the angle between each fracture and the mylonitic foliation (ω); (4) the width of a grain in the direction of each given fracture (w); (5) the actual length of each fracture (b), $b = w$ for transgranular fractures and $b < w$ for intragranular fractures; and (6) the normal distances between a fracture and its two nearest neighbors (f_1 and f_2). In addition, special attention was paid to determining whether the fractures in garnet grains extend into their surrounding matrix minerals such quartz, feldspar and sillimanite.

The grain size (d) and aspect ratio (s) of each garnet grain are calculated respectively by

$$d = 2\sqrt{Lr_0} \tag{1}$$

and

$$s = L/r_0. \tag{2}$$

In Fig. 6(a & c) linear histograms showing frequency distributions of d and s of garnet, respectively, are given. The mean d and s values are greater than the mode and median values, which indicates that the distributions of grain size and aspect ratio are skewed with the right tail of the distributions longer than the left tail (Figs 6a & c).

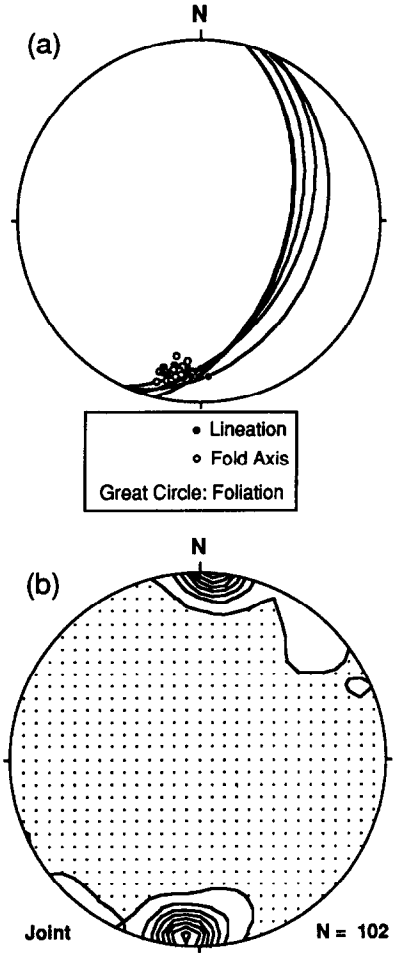

Fig. 2. Stereoplots of structural data measured from a typical outcrop. (a) Mylonitic foliations and lineations and fold axes; and (b) joints.

The distribution of s is truncated at values less than 1 because the aspect ratio is defined as the ratio of the maximum length to the maximum width. Figure 6(b & d) are histograms of the natural logarithms of d and s for the same data, and show that the grain size and aspect ratio of garnet may be approximately described by a log-normal distribution. It is noted that 34% of the garnet grains have an aspect ratio larger than 2 while only 33% have an aspect ratio less than 1.5. Garnet crystals from quartzitic, granitic and charnockitic mylonites are more elongate than those from paragneiss and mafic granulite. The elongate garnet crystals are oriented with their longer axis parallel to the mylonitic foliation. The origin of these flattened garnets has been discussed in Ji and Martignole (1994, 1996).

The mean fracture spacing (m) of a given grain is calculated according to

$$m = \frac{2L}{n+1} \tag{3}$$

where n is the total number of fractures across the garnet elongation direction.

The aspect ratio of fractured segments (s_f) can be calculated from w and f_1 or f_2 data,

$$s_f = f_1/w. \tag{4}$$

Principal characteristics of the fractured garnets are as follows.

(1) In a garnet crystal, the fractures can either cut across the entire grain (transgranular) or terminate inside the grains (intragranular) (Figs 3 & 4). Statistical studies (Fig. 7a) show that 51% of the garnet microfractures are transgranular and 49% are intragranular. Both types of fractures are generally straight rather than curvilinear (Figs 3 & 4) and form quasi-parallel arrays. The intragranular microfractures commonly taper from the grain boundary towards the core, indicating that these microcracks were initiated at the grain boundaries and then propagated inwards for different distances towards the grain centers. Our measurements show that about 36% of the microfractures propagated inwards for a distance less than the half width of a grain (Fig. 7a). Some fractures appear to have started and propagated from the boundaries of inclusions (mainly quartz) within the garnets since few inclusions are cut through by fractures (Figs 3e & 4a–c). These indicate that interfaces between different phases are mechanical and structural heterogeneities that control the initiation of fractures. Cracks might originate independently at each side boundary of a garnet crystal and propagate inward, forming a single transgranular crack or two overlapping cracks (Figs 3c & d). Single intragranular fractures that have their two ends terminating in the interior of a garnet are also observed locally (Fig. 3b). Some cracks have a curving-perpendicular geometry (Rawnsley *et al.*, 1992) at abutments with the nearest fractures (e.g. Figure 4c).

(2) About 85% of individual fractures are confined to the host garnet, including both transgranular and intragranular fractures (Figs 3a, b, e & 4), while about 15% of fractures extend into the surrounding matrix minerals (e.g. mainly quartz and sillimanite) (Fig. 3c & d). The fractures in quartz grains are always healed and may be recognized by the alignment of bubbles which are either fluid inclusions or mineral precipitates deposited when the microfractures were open to pore fluids during or after fracturing. No grain-boundary fractures are observed, indicating a high interfacial strength in the rocks (Lloyd and Knipe, 1992).

(3) Fractures within garnet crystals are pervasively developed and are relatively straight, single-strand cracks (Figs 3 & 4). There is no evidence showing that the crack surfaces in garnet grains have been eroded or modified by dissolution.

(4) Elongate and/or small garnet grains generally develop only a set of tensile fractures perpendicular to foliation and lineation (Fig. 3a–d) while large and/or equant garnet grains usually develop two sets of tensile fractures (Figs 3e & 4a–d). Figure 7(b) shows that about 80% of the fractures are perpendicular and 20% are parallel to the foliation and lineation. Both sets are best observed in the sections cut perpendicular to the foliation

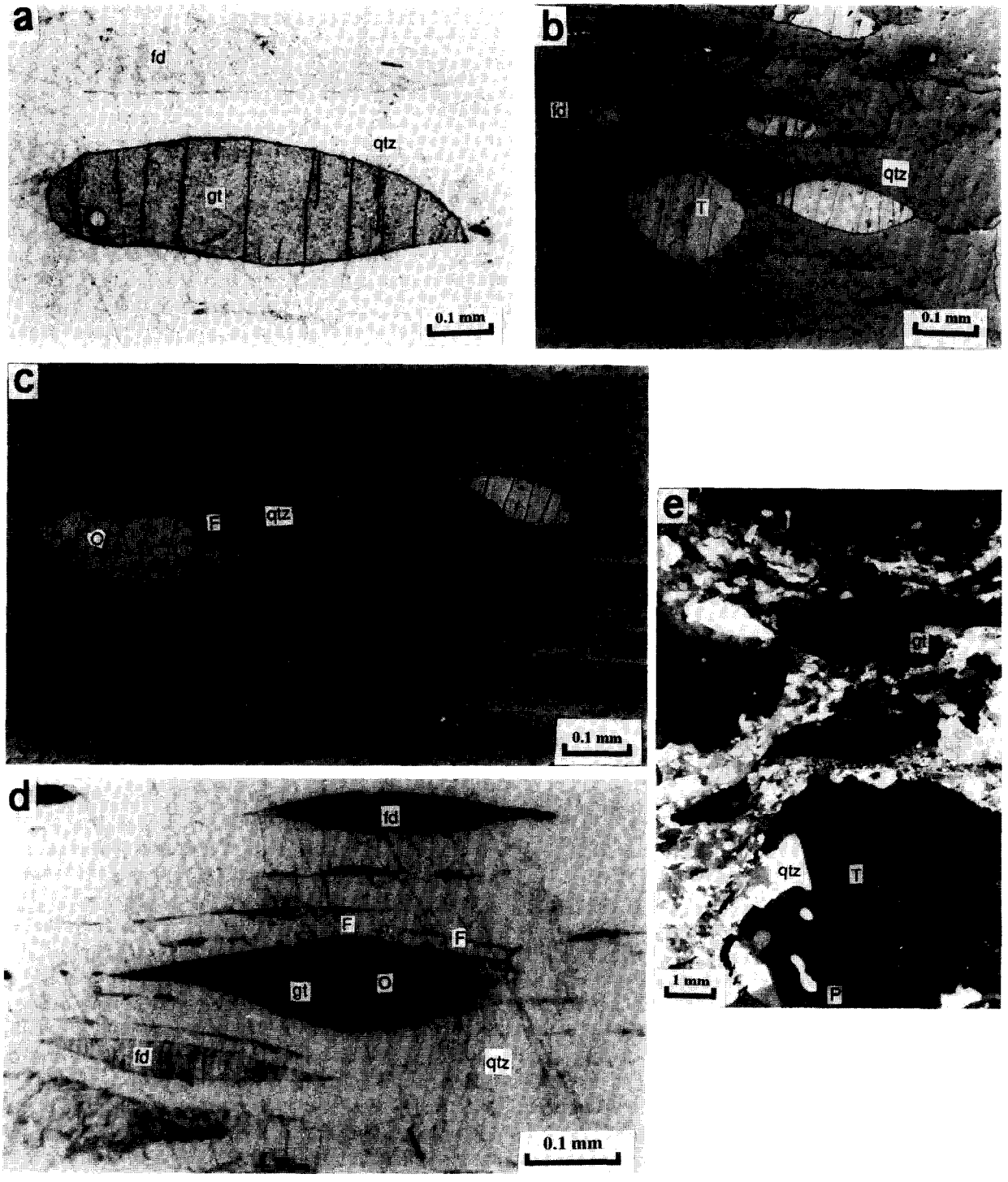

Fig. 3. Photomicrographs of X–Z sections of fractured garnet crystals in the quartzitic layers of granitic mylonites (a–d) and in the paragneissic mylonite (e). (a), (d) and (e) transmitted light; (b), (c) reflected light. gt, garnet; fd, feldspar; qtz, quartz. Overlapping fractures (O) in (c) and (d); cracks with their ends terminating in the grain interior (T) in (b) and (e); fractures extending from garnet crystals into the surrounding felsic matrix (F) in (c) and (d). Only one set of tensile fractures are developed in (a)–(d). In (e), both lineation-perpendicular and foliation-parallel fractures are developed, and some foliation-parallel fractures cross-cut one or several lineation-perpendicular fractures (P).

and parallel to the lineation (Figs 3e & 4a–d). The lineation-perpendicular (LP) fractures are more planar and regular than the foliation-parallel (FP) cracks. Within a variance of $\pm 15°$, the LP fractures are mutually parallel, and parallel to those in all other garnets in the same sample and even in the same outcrop. The FP cracks usually abut against the nearest LP fractures, forming a ladder-like pattern. Some FP cracks cross-cut one or several LP fractures before abutting (Fig. 3e). The frequent abutments of FP cracks against LP fractures suggest that the FP cracks are younger than the LP fractures. The occurrence of two

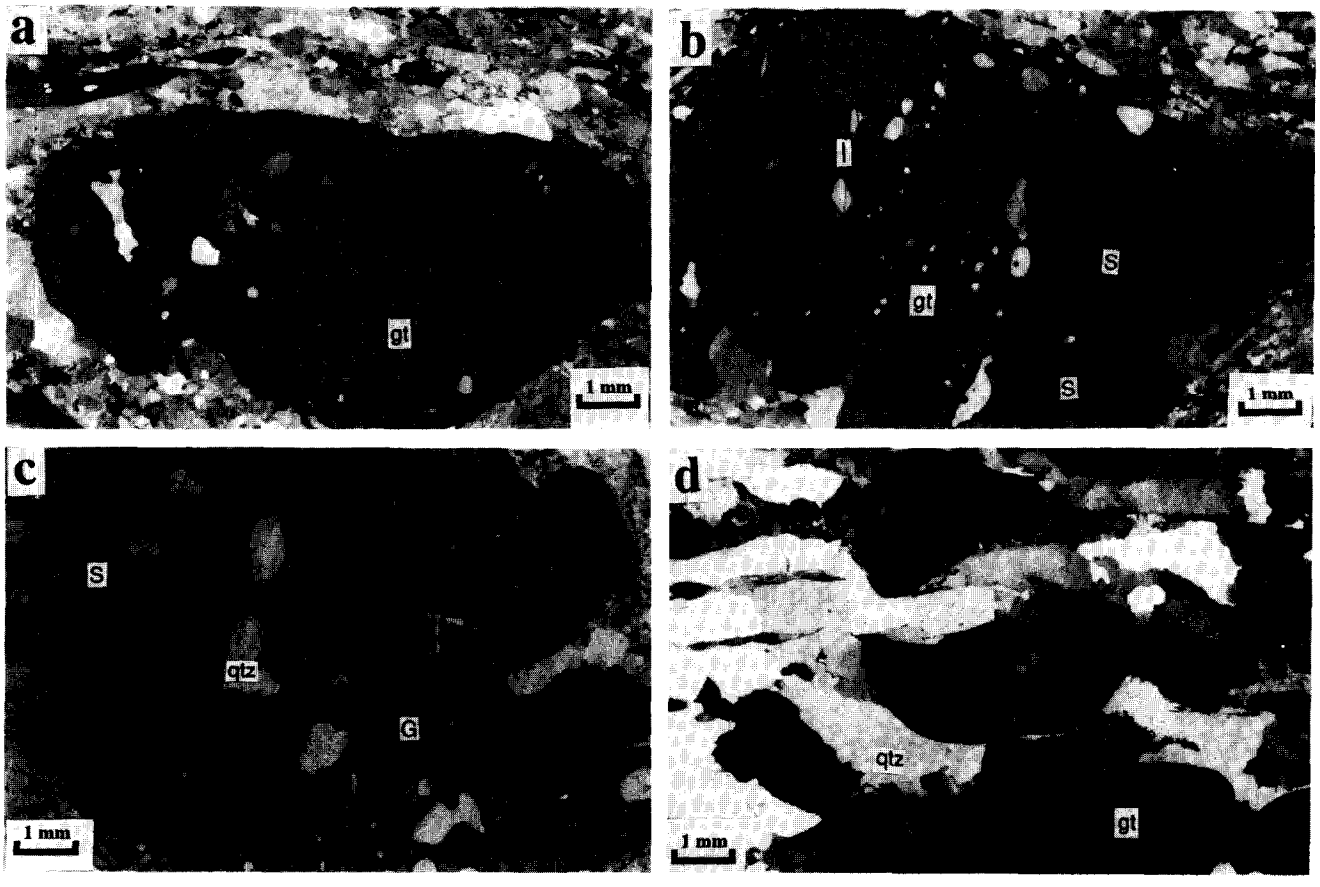

Fig. 4. Transmitted light photomicrographs of X–Z sections of fractured garnet crystals (gt) in the paragneissic mylonites (X parallel to the longer side of photographs). Quartz (qtz) inclusions in the garnet crystals are not cut through by fractures except at I in (b). Lineation-perpendicular fractures (predominant) are more planar and regular than foliation-parallel fractures (secondary). Foliation-parallel fractures usually abut against the nearest lineation-perpendicular fractures (S). Curving-perpendicular geometry defined by Gross (1993) (G).

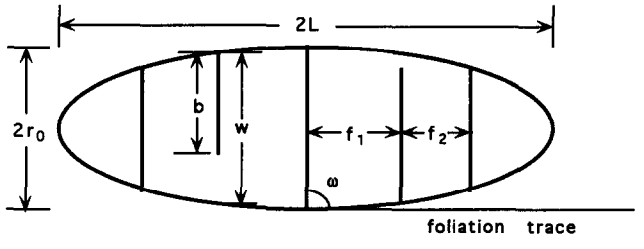

Fig. 5. Schematic diagram to illustrate the parameters measured for statistical analysis. See text for details.

perpendicular sets of tensile fractures in garnet crystals from a gabbro-derived amphibolite at Gore Mountain (Adirondacks, New York) was reported by Valentino and Sclar (1981).

(5) Based on our observations of thousands of microfractures, no microfractures were seen to offset grain boundaries or any other features such as inclusions within garnet grains, even down to the microscopic scale. For a given fracture, its two fracture walls are almost always parallel to each other rather than in a V-shape (Hippertt, 1993; Michibayashi, 1996), suggesting that neither rotation of the fractured segments nor displacement oblique to the fracture normal occurred after microfracturing. Moreover, no en échelon arrays of fractures are found in the garnet grains. Thus, the fractures in garnet are extensional mode I fractures.

(6) The crack planes are very sharp and no ductile deformation is visible at their edges, suggesting that the garnet was brittle when cracking took place. The fractures are generally only several micrometres wide and appear as hairline fractures under the optical microscope. The fractured parts of each garnet grain have not been separated or filled with matrix minerals such as quartz and feldspar. This indicates that the mylonitic matrix was not plastically flowing during and after the fracturing of garnets. A stiff crystal such as garnet which fractured while located in a still active ductile shear zone would be rapidly disrupted by continued plastic deformation of its quartzo-feldspathic matrix (Lloyd *et al.*, 1982; Ji and Zhao, 1993). The fracturing is interpreted to take place at temperatures lower than 300°C, below which the quartzo-feldspathic matrix would not be capable of plastic flow at geologically reasonable strain rates. The upper limit of the quasi-plastic zone in quartzo-feldspathic crust generally corresponds to the critical temperature (300°C) for thermal activation of intracrystalline creep in quartz at natural strain rates (Scholz, 1990). Therefore, the garnets were fractured at shallow crustal depths

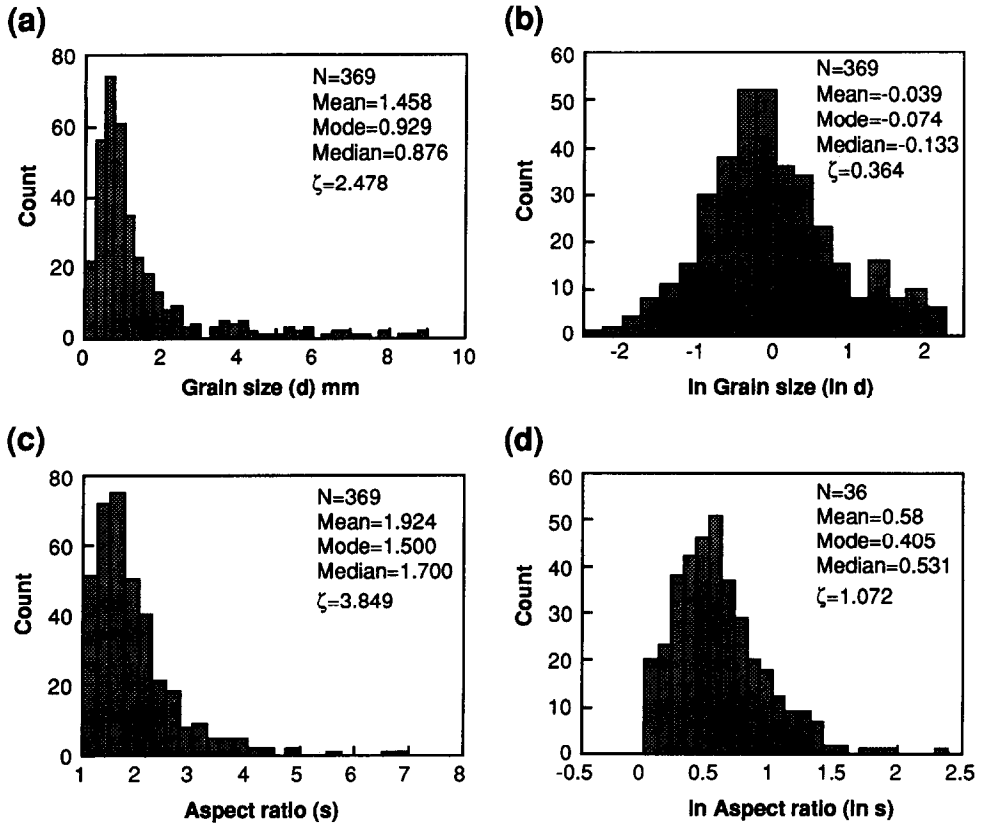

Fig. 6. Frequency distributions of garnet grain size (a and b) and aspect ratio (c and d) in the studied mylonites; (a) and (c) linear scale; (b) and (d) natural log scale. ζ, skewness; N, number of measurements.

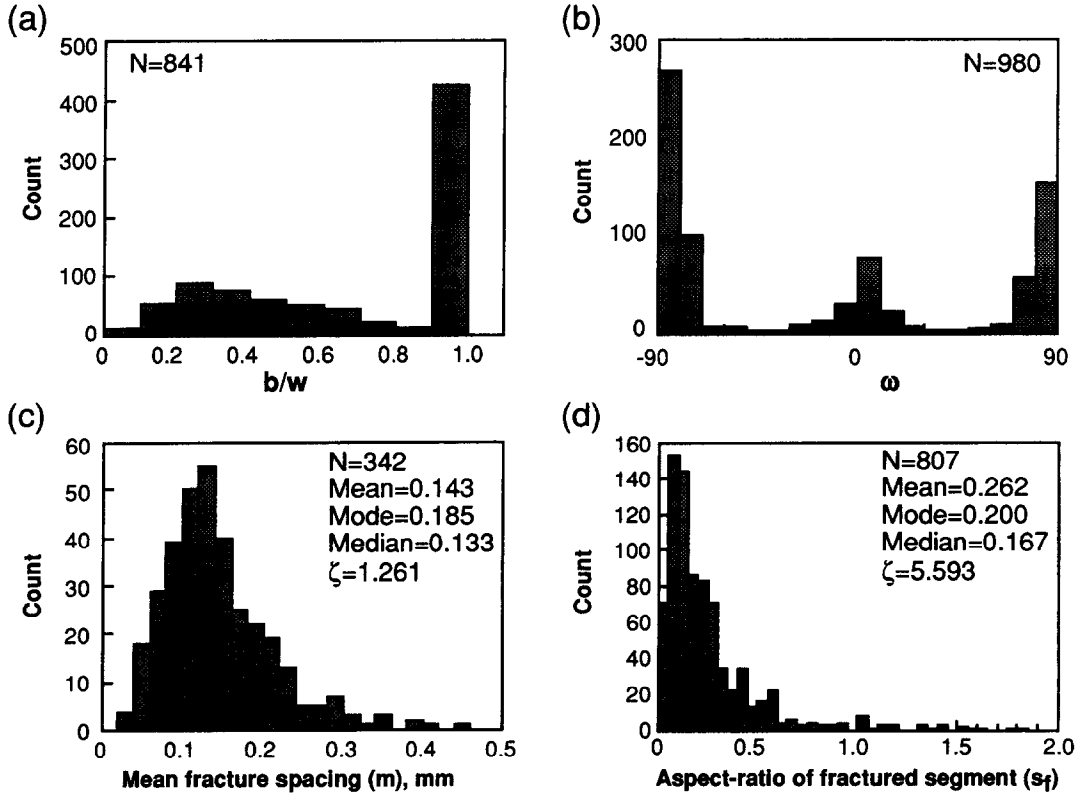

Fig. 7. (a) Frequency distributions of b/w ratio; (b) preferred orientation of the garnet fractures with respect to the foliation and lineation (0° position); (c) mean fracture spacing; (d) aspect ratio of the fractured segments. ζ, skewness; N, number of measurements.

(< 15 km for a thermal gradient of 20°C/km). In addition, the fractures are generally very clean, with no retrograde materials (e.g. biotite, muscovite and chlorite), indicating that fracturing occurred at low temperature.

(7) The total fracture length (y) within a garnet grain increases with increasing grain size (d) or the length of the longer axis ($2L$) and appears to follow a power law (Fig. 8): $y = Ad^i$ or $y = B(2L)^j$, where A, B, i and j are constants. The distribution of fracture spacing is generally single-peaked, although skewed to some extent (Fig. 7c). Variations in fracture spacing with respect to grain size, aspect ratio and garnet spacing are complex. Generally speaking, the larger grains have a larger mean fracture spacing and the grains with larger aspect ratios have smaller mean fracture spacing. For an individual grain, the fracture spacing generally reduces with decreasing diameter from the center to the two ends (Figs 3a, b, d & 9). In addition, fracturing becomes intensive in regions where the garnet crystals are very close together in a cluster (Fig. 3e). Although the garnet grains generally are not in contact with each other, mechanical interactions between them result in local stress concentrations at the garnet clusters. Drucker (1965) noted that in particle-reinforced metal–matrix composites, matrix deformation between closely spaced strong particles is highly constrained, resulting in local stress levels several times higher than the far-field matrix stress. This behavior has recently been confirmed by finite-element modeling (Watt *et al.*, 1996).

(8) Grains with larger grain size and/or large aspect ratio are favorable for tensile fracturing (Fig. 10). Fractures in grains smaller than 0.2 mm with an aspect ratio less than 2 are rare. A similar effect of particle size on particle cracking has been well documented for two-phase industrial composites (e.g. Al–SiC system; Lloyd, 1991; Li and Ellyin, 1995) and for granitic mylonites (Ji and Zhao, 1993; Michibayashi, 1996). They found that in populations with a large range in size, it is the largest particles which tend to fracture. Since the internal tensile stress in a stiff grain such as garnet is approximately independent of size, this effect can be attributed to a size dependency of fracture toughness. A large grain contains more and larger flaws than a small grain (Lloyd, 1991).

EXISTING MODELS RELATED TO GARNET FRACTURES

Our microstructural observations suggest that a model to explain the origin of the garnet fractures must account for: (i) restriction of the fracture arrays to garnet; (ii) the pervasive, non-random spacing of the fractures; and (iii) the systematic orientation of the fractures with respect to the foliation and lineation of the rocks. The following discussion relates only to the origin of the garnet fractures from the MSZ, although there are obvious implications for tensile fractures of minerals in similar environments elsewhere.

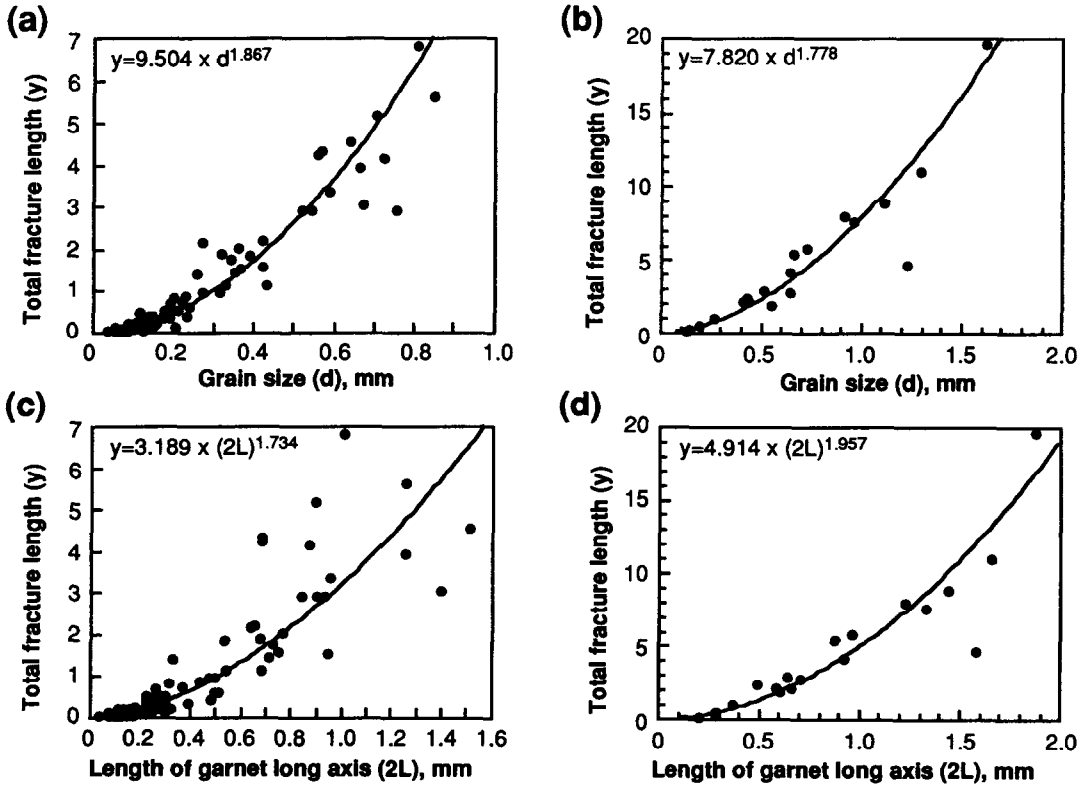

Fig. 8. Variation in the total fracture length within a given garnet grain as a function of grain size (a and b) and long axis length (c and d).

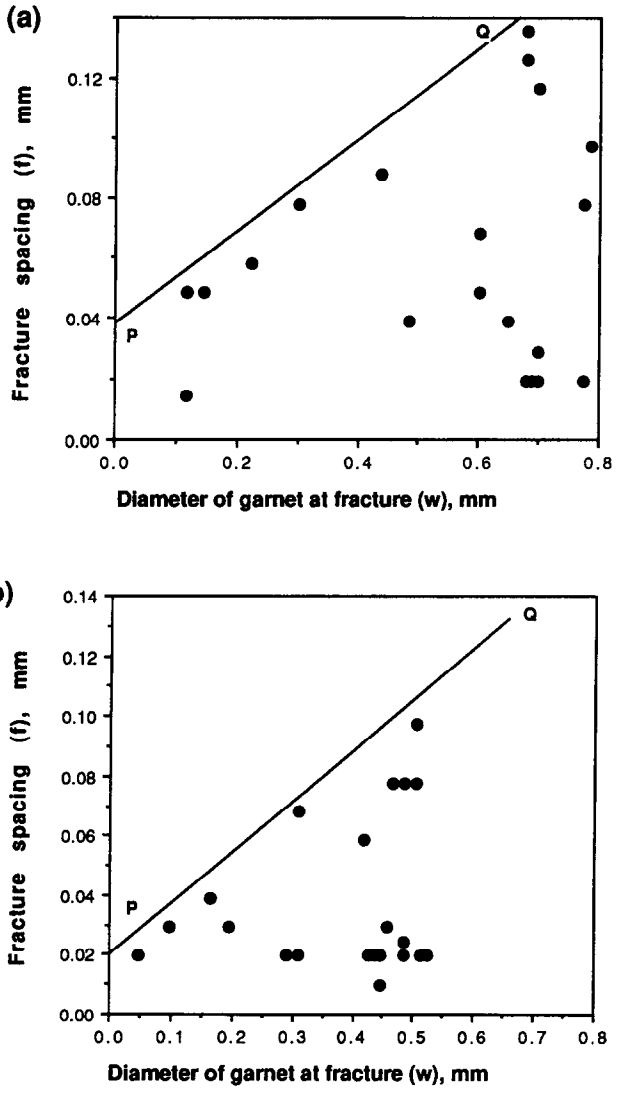

Fig. 9. Variation in fracture spacing as a function of the diameter of garnet at position of fracture for two garnet grains (a and b). No points plot above line PQ, indicating a non-random distribution of fracture spacing.

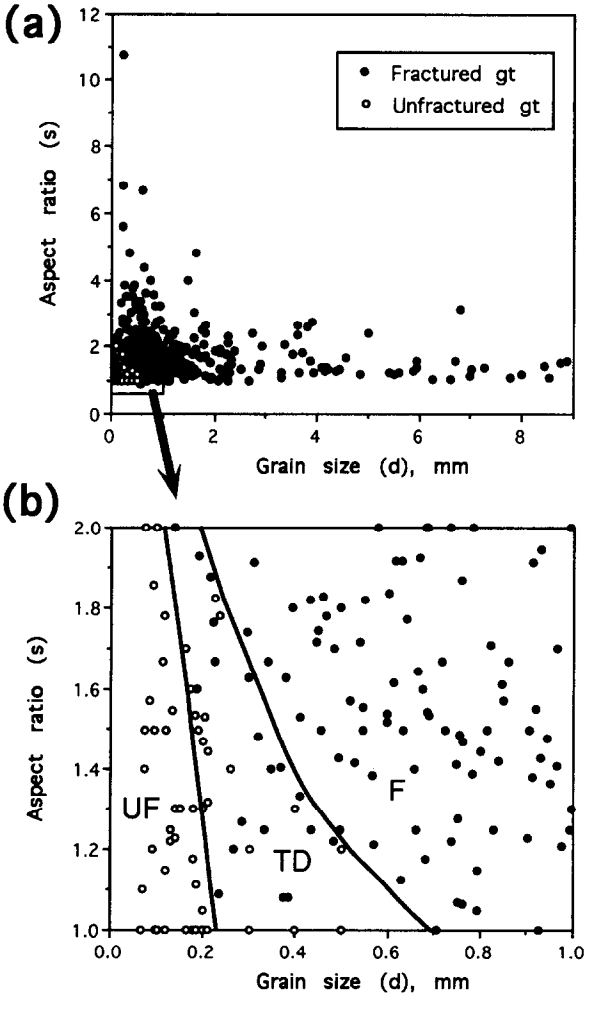

Fig. 10. Data showing the influence of grain size and aspect ratio on tensile fracture of garnet (gt). Almost no fractures are found in the grains smaller than 0.2 mm with an aspect ratio of less than 2. F, UF and TD stand for fractured, unfractured and transition domains of garnet, respectively.

Fracture induced by residual stresses

Rocks are polycrystalline aggregates in which different minerals generally have different thermal expansion coefficients and elastic stiffnesses. As a result of this thermoelastic heterogeneity, misfit (or residual) stresses are generated because each phase expands or contracts differently in response to changes in temperature and pressure, phase transformation, inelastic deformation and initial stress. For an isolated inclusion with an arbitrary shape embedded in an infinite elastic matrix, analysis of the stresses in the inclusion and the surrounding matrix can only be carried out numerically, but for the special case of an ellipsoid (Eshelby, 1957, 1959; Mura, 1982) or a sphere (Holzhausen and Johnson, 1979; van der Molen, 1981; Gillet *et al.*, 1984; Lee and Tromp, 1995) an analytical solution can be found. The models predict that the stresses in a spherical inclusion are uniform and the stress field in the matrix is eccentrically symmetric if the stresses applied to the matrix at infinity are hydrostatic. Upon cooling, for example, an inclusion with a smaller thermal expansion than the matrix will generate circumferential tensile stresses and promote radial cracking. In contrast, an inclusion with a greater thermal expansion than the matrix will generate radial tensile stresses and promote circumferential cracking. A volume increase due to a phase transformation of the inclusion during unloading and cooling (e.g. from coesite to α-quartz) will also generate circumferential tensile stresses resulting in radial cracking. This has been considered as the mechanical origin of radial tensile cracks around coesite or former coesite inclusions in garnet from ultra-high-pressure metamorphic terranes (e.g. Chopin, 1984; Zhang *et al.*, 1995) and in metamict zircon (Lee and Tromp, 1995). Recently, Wendt *et al.* (1993) found that radial cracks around quartz inclusions in garnet from high-*P* metapelitic rocks (1.0–2.0 GPa, 450–600°C) in Oman formed during uplift entirely within

the stability field of α-quartz. Their data demonstrate that quartz dilates more than its surrounding garnet during uplift. For the same reason, we would have observed either concentric fractures in garnet grains embedded in the matrix of quartz or radial cracks around quartz inclusions within garnet. Therefore, the existing models cannot be used to interpret the origin of the fractures in the garnet from the MSZ because: (i) they are neither radial nor concentric; (ii) they are not randomly spaced and thus cannot be explained by the assumption of uniform stress in the inclusion; and (iii) they occur in garnet grains both with and without inclusions.

Microcracking resulting from internal stresses between grains due to incompatible strains from either thermal expansion or elastic anisotropy has been well studied by materials scientists. Both the experimental (Cleveland and Bradt, 1978; Rice and Pohanka, 1979) and theoretical (Evans, 1978; Tvergaard and Hutchinson, 1988) investigations demonstrate that such cracking occurs principally along grain boundaries and initiates primarily at triple points (locations where three grains come into contact) where the maximum tensile stress concentration is located. Experiments by Fredrich and Wong (1986) on Westerly granite at room pressure and temperature between 250 and 620°C show that after most of the grain boundaries have already cracked, intragranular or transgranular cracking may occur in feldspar, but not in quartz. They attribute such a discrepancy to the fact that feldspar has well-developed cleavages while quartz has not. Obviously, the above model cannot explain our observations that cracks are intragranular and transgranular, and restricted to the stiff garnets lacking cleavage, whereas the feldspar in the same rock is not cracked. In addition, no cracks along grain boundaries are observed in the studied rocks.

The release of residual stresses during natural or artificial excavation may generate the so-called rebound fractures such as sheet structure and exfoliation in rock masses (Nichols, 1980; Suppe, 1985). The rebound fractures are generally parallel to the topographic surface and independent of the foliation and lineation. In contrast to the sheet structure and exfoliation described by previous authors (Holzhausen and Johnson, 1979; Suppe, 1985; Prior and Behrmann, 1990), the fractures described in this paper are restricted in garnet crystals and preferentially perpendicular to the (subhorizontal) lineation (Fig. 2). Thus, associated inferences of rebound fracture processes cannot be made here.

Fluid-assisted dissolution-precipitation

Prior (1993) studied fractures in garnets from the Alpine Fault mylonites and suggested that the fractures were propagated by fluid-assisted dissolution-precipitation at high-stress crack tips under greenschist–amphibolite-facies conditions. However, the garnet fractures studied by Prior (1993) are irregularly distributed, highly variable in orientation and filled either with new garnet grains or with retrogressive assemblages such as quartz–chlorite–plagioclase ± biotite ± muscovite. This microstructure differs substantially from that described here, so that the fracture process proposed by Prior (1993) is unlikely to apply to the garnets from the MSZ.

Hydraulic fracture

Ladeira and Price (1981) proposed a hypothesis involving the pore fluid pressure to explain fractures in rocks. This hypothesis is described as follow: when a fracture forms, the pore fluid pressure in the neighborhood of the fracture decreases as pore fluid flows into the open fracture. As the pore fluid pressure declines, the effective Mohr circle moves away from the failure criterion, so further fracture in the vicinity of the initial fracture is impossible. A second fracture can form in the rock only beyond the zone of reduced pore pressure, thereby defining the minimum spacing for the formation of hydrofractures. This hypothesis predicts that the fracture spacing depends on the permeability of the rock, so highly permeable rocks should have a larger fracture spacing than less permeable rocks. The permeability is almost zero in unfractured single crystals of garnet. The average fracture spacing in the studied garnet grains is only 0.14 mm (Fig. 7c) while the average fracture length is 3–5 times higher than this value (Fig. 7d). Moreover, the fractures formed in the brittle upper crust with a good permeability due to the high connectivity of fluid-migration pathways along foliation-parallel cracks. In such an environment the fluid pressure should remain near-hydrostatic (Reynolds and Lister, 1987). Furthermore, there is no diagnostic evidence for the operation of a hydraulic fracture mechanism, such as garnet fragments detached from fracture walls and floating in the retrogressive fracture filling (Prior, 1993). Thus, the closely spaced fractures in the studied garnet cannot be interpreted by the hypothesis involving the pore fluid pressure.

PROPOSED MODEL FOR THE GARNET FRACTURES

Source of tensile stresses

It is necessary to analyze the source of tensile stresses which caused the garnet fractures. As described before, the garnet fractures are preferentially oriented normal to the subhorizontal stretching lineation irrespective of its trend. This suggests that the orientation of fracture arrays was controlled by the anisotropic response of the mylonites to a far-field tensile stress in the horizontal plane. Because no geological data indicate any significant tectonic activity in the region after the granulite-facies metamorphism, the simplest and most widely acceptable geological event which might result in such a horizontal stress is unloading and cooling. Moreover, the garnet

fractures formed at shallow depths where all constitutive minerals of the mylonites such as feldspar, quartz and garnet behaved elastically and brittlely. In other words, they formed during uplift and cooling of previously ductilely deformed mylonites and gneisses within the upper crustal environment.

The horizontal stress (σ_H) at a given depth (H_f) within the brittle portion of the crust can be approximately estimated from the following equation (Haxby and Turcotte, 1976):

$$\sigma_H = \left(\frac{\nu}{1-\nu}\right)\rho_c g H_f + \left(\frac{E}{1-\nu}\right)\alpha\frac{dT}{dz}\Delta H + \frac{E}{(1-\nu)}\frac{\rho_c}{\rho_m}\frac{\Delta H}{(R-\Delta H)} \quad (5)$$

where ν, ρ_c, E and α are the Poisson ratio, density, Young's modulus and coefficient of thermal expansion of crustal rock, respectively; g is the gravitational acceleration; dT/dz is the thermal gradient; R is the radius of the Earth, 6370 km; ρ_m is the density of mantle rock; and ΔH is the incremental change in depth due to uplift and erosion. Equation (5) is derived using a uniaxial strain model which assumes that the rock cannot freely extend or contract horizontally because to do so it would have to separate from the adjacent rock (Haxby and Turcotte, 1976; Bruner, 1984). The first term of equation (5) describes a horizontal compressive stress induced by the vertical load ($\rho_c g H_f$) due to the Poisson effect. The second and third terms of equation (5) describe two horizontal tensile stresses which are related to a thermal contraction upon cooling and to a change in the radial distance from the Earth's center due to the vertical uplift, respectively. As the radial distance increases, the arc length increases from deep to shallow depths.

Equation (5) predicts that as long as the absolute value of ΔH is large enough, the horizontal stress σ_H becomes tensile. Figure 11 shows variations of σ_H as functions of ΔH and H_f, calculated using $E = 97{,}000$ MPa, $\nu = 0.25$, $\alpha = 3 \times 10^{-5}$/°C (Turcotte and Schubert, 1982, p. 179) and $dT/dz = 20$°C/km. The critical value of ΔH for the switch from compressive to tensile stresses increases with increasing H_f. The tensile strength of minerals generally decreases with decreasing confining pressure due to removal of overburden (Price and Cosgrove, 1990). Thus, tensile fracturing is easier at shallow than deep depths. If the horizontal tensile stress (negative) is smaller than or equal to the tensile strength of the rock (e.g. 40 MPa, Price and Cosgrove, 1990), vertical fractures or joints that are normal to this stress will form. At a depth of 5 km, for example, an incremental uplift of 1 km can cause a generation of tensile fractures (Fig. 11).

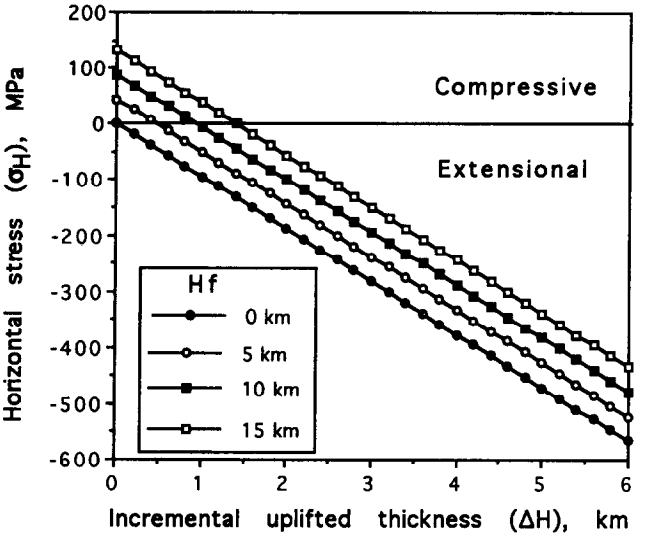

Fig. 11. Variation in horizontal stress as a function of incremental uplifted thickness (ΔH) and depth at which fractures are initiated (H_f). The horizontal stress can be switched from compressive to extensional as long as ΔH is large enough.

Cause for the preferred orientation of garnet fractures

The fracture orientation appears to have been controlled by the elastic anisotropy of the mylonitic rocks. We measured P-wave velocities of a representative paragneissic mylonite and a typical garnet-bearing quartzitic mylonite in the directions parallel to lineation and normal to foliation at hydrostatic confining pressures up to 600 MPa (equivalent to crustal depths of approximately 20 km) and at room temperature. The mini-cores cut from the rock samples for velocity measurements are 2.5 cm in diameter and 5.0 cm in length. The velocity measurements were made on dry, jacketed samples using the pulse transmission technique (Birch, 1960). P-waves were generated and received by 1 MHz lead zirconate piezoelectric transducers. Errors in ultrasonic velocity measurements are generally regarded to be less than 1% (Christensen and Shaw, 1970). There is a rapid increase in velocity up to about 100 MPa (Fig. 12a & c), which is related to the closing of cracks (Birch, 1960). From 100 to 600 MPa, velocity increases almost linearly with increasing pressure, reflecting the intrinsic properties of the rock. P-wave velocity is significantly higher along the lineation (X) than normal to the foliation (Z). This indicates that the mylonites and gneisses are more compressible in the Z- than in the X-directions, that is E (Young's modulus) is larger in X than in Z. The seismic anisotropy (A) is defined as: $A = 100\%(V_{max} - V_{min})/V_{mean}$ (Birch, 1960). As shown in Fig. 12(b & d), the seismic anisotropy increases with decreasing confining pressure below 200 MPa ($< \sim 8$ km) and is almost constant ($A = 3$–4%) at confining pressures higher than 200 MPa. At confining pressures below 200 MPa, the seismic anisotropy reflects mainly the behavior of foliation-parallel fractures in rocks, but at higher confining pressures the cracks are closed and the seismic anisotropy reflects mainly crystallographic preferred orientation of minerals in the rocks (Ji *et al.*, 1993).

According to equation (5), the far-field tensile stress σ_H increases with increasing E. In the case of a strike-slip ductile shear zone (e.g. the MSZ) where lineation is

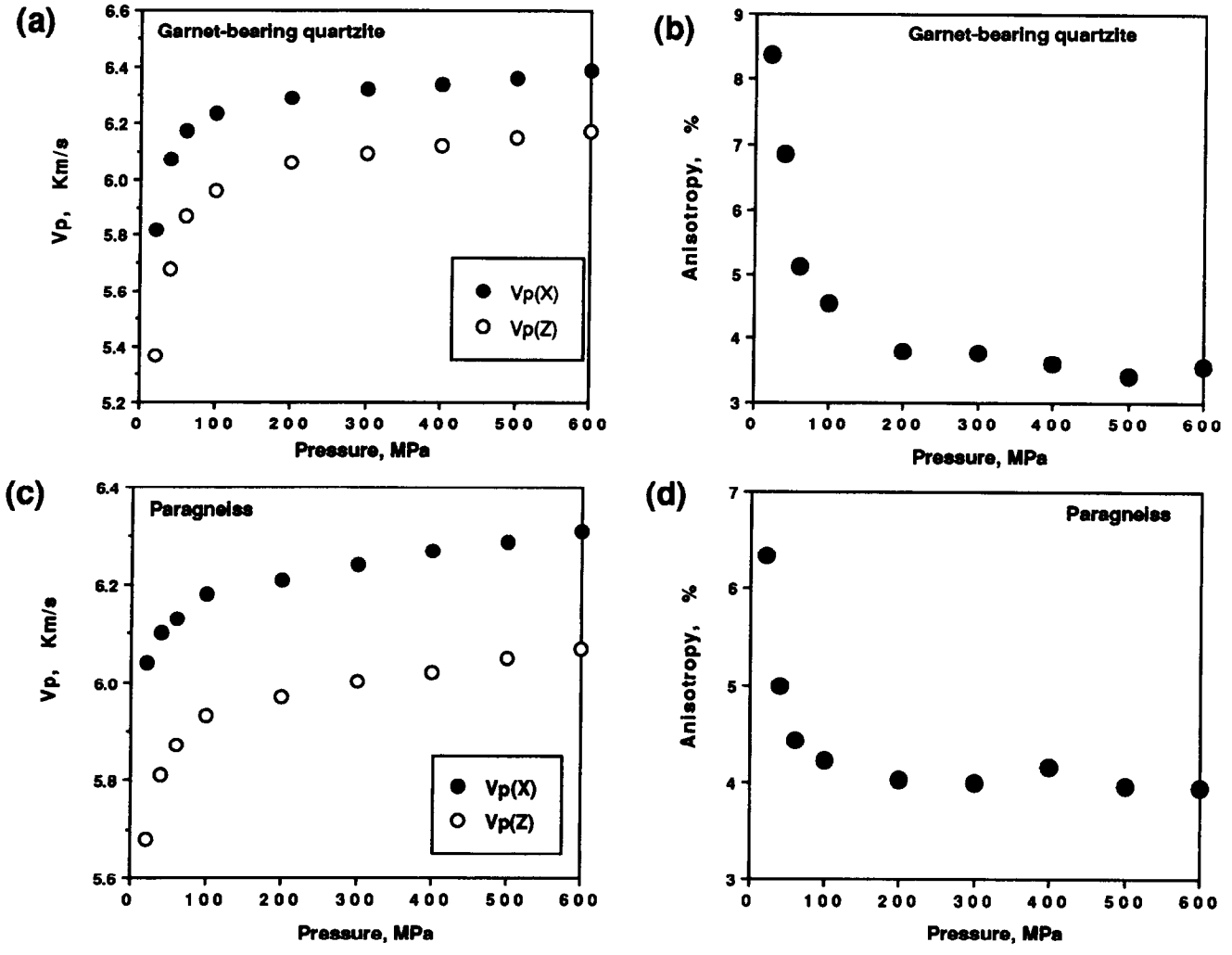

Fig. 12. P-wave velocities as a function of confining pressure for the directions parallel to the extension lineation and perpendicular to the foliation in a garnet-bearing quartzite (a) and a paragneiss (c). P-wave velocity anisotropy increases with decreasing confining pressure (b and d).

subhorizontal, E and thus σ_H are larger along the lineation direction than normal to the foliation. The mylonites could readily accommodate the elastic stretching normal to the foliation, whereas within the plane of foliation, the mylonites would be less able to accommodate the imposed elastic extension. Consequently, the tensile stress in the direction parallel to foliation and lineation could be high enough to break brittle minerals such as garnet. Because the difference in E value between the X- and Z-directions decreases with increasing confining pressure, the dominance of fractures normal to the foliation should imply that the fractures formed at shallow depths. This conclusion agrees with that derived from our microstructural observations.

Shear-lag model

Since the tensile strength of garnet may be higher than that of quartz and feldspar, the fracturing should take place preferentially in quartz and feldspar. In the following, we will analyze why tensile fracturing took place preferentially in garnet using the shear-lag model.

The shear-lag model or stress transfer model was originally developed by Cox (1952) and later refined by Holister and Thomas (1966) and Kelly and Macmillan (1986) to predict the distribution of tensile stress along a *cylindrical* fiber and shear stress at the interface between the fiber and matrix in a two-phase composite. This theory assumes that if no slip occurs on the phase interfaces, the presence of the fiber redistributes the stresses and strains within the composite material and has an effect of transferring load from the matrix to the fiber. This process has two corollaries: (i) a shear stress occurs at the fiber–matrix interface; and (ii) the harder phase carries a comparatively greater part of the stress, while the soft phase tends to take the greater part of the strain (with reference to the volume fraction ratio). This model has been widely used by material scientists and structural geologists to analyze extension fracture boudins (Lloyd *et al.*, 1982; Masuda and Kuriyama, 1988; Ji and Zhao, 1993), and to predict flow strengths of two-phase rocks (Ji and Zhao, 1994) and industrial composites (e.g. Kelly and Street, 1972; McLean, 1972; Nardone and Prewo, 1986).

The classic shear-lag model considers a basic unit cell consisting of a long, cylindrical fiber embedded completely in a continuous incompetent matrix, which is subjected to a remotely applied tensile loading. According to Kelly and Macmillan (1986), the axial tensile stress [$\sigma(x)$] in the fiber is given by

$$\sigma(x) = E_f\varepsilon\left[1 - \frac{\cosh[\beta(l/2 - x)]}{\cosh(\beta l/2)}\right] \quad (6)$$

where E_f and l are the Young's modulus and the length of the fiber, respectively; ε is the tensile strain of the unit cell along the fiber alignment direction (x); and

$$\beta = \frac{2s}{l}\sqrt{\frac{-2E_m}{E_f(1+\nu)\ln(V_f)}} \quad (7)$$

where s is the aspect ratio of the fiber, E_m and ν are the Young's modulus and Poisson ratio of the matrix, and V_f is the volume fraction of fiber in the composite.

Equation (6) cannot be used for estimating the tensile stress in a short fiber ($s < 10$) since the derivation of this equation is based on an assumption that no load transfer occurs from the matrix to the end faces of the fiber. For a short fiber, the load transfer at the ends cannot be ignored and should be equal to $\pi r^2 E_m\varepsilon$. The distribution of tensile stress in the short fiber as a function of distance (x) is then given by Ji and Zhao (1994) as

$$\sigma(x) = E_m\varepsilon\left\{\frac{E_f}{E_m} + \left(1 - \frac{E_f}{E_m}\right)\frac{\cosh[\beta(l/2 - x)]}{\cosh(\beta l/2)}\right\} \quad (8)$$

In equations (6) and (8), $\varepsilon = \varepsilon_a + \varepsilon_t$, where ε_a is the strain due to the applied external tensile stress, and ε_t is the mismatch strain due to the differences in coefficients of thermal expansion between the fiber and matrix. Neglecting the radial strains, which are small compared to the axial strains for a slender body (Dunand and Mortensen, 1991), we have

$$\varepsilon_t = (\alpha_m - \alpha_f)\Delta T \quad (9)$$

where α_m and α_f are, respectively, the matrix and the fiber coefficients of thermal expansion, and ΔT is the temperature change. In the present study, ε_t can be neglected since there is only a minor difference in the coefficients of thermal expansion between α-quartz (24.3×10^{-6}/°C) and garnet (20.6×10^{-6}/°C) in the range of temperature from 25 to 500°C (Fei, 1995). Hence, the tensile stresses resulting in fracturing of garnet were derived from far-field tensile stresses rather than from the thermal mismatch stresses between garnet and the surrounding matrix (mainly quartz) upon cooling.

Equation (8) predicts that the tensile stress $\sigma(x)$ increases from $E_m\varepsilon$ (the tensile stress of the matrix) at the ends of the fiber to a maximum at the center, so that fracture will occur at the mid-point of the fiber. However, most stiff minerals in deformed mylonites have a lenticular or ellipsoidal shape rather than a perfect cylindrical shape; their cross-sectional area is variable along their length (Ji and Zhao, 1993). Thus, the tensile stress distribution and resulting fracture location in flattened garnets cannot be correctly predicted by equation (8).

In order to do so, we develop a new mechanical model (see Appendix for details) for an inclusion–matrix system based on fundamental assumptions of the shear-lag model (Cox, 1952; Holister and Thomas, 1966; Kelly and Macmillan, 1986). The inclusion is represented by a rotation body with any given longitudinal section (e.g. lens, ellipsoid or truncated ellipsoid). The axial tensile stress in the inclusion as a function of distance along the long axis (i.e. x-direction in Fig. A1) can be obtained by numerically solving a differential equation (equation (A14) in the Appendix) if the material constants E_f, E_m and ν are known. In the present case, $E_f = 3.09 \times 10^5$ MPa for garnet. If the matrix is quartz, $E_m = 9.70 \times 10^4$ MPa, $\nu = 0.08$. If the matrix is plagioclase, $E_m = 1.16 \times 10^5$ MPa, $\nu = 0.30$. Our calculation results for a lenticular garnet using these elastic constants, $\varepsilon = 0.5\%$, $s = 4$ and $V_f = 7\%$, are shown in Fig. 13. The values of the elastic constants given above were obtained from laboratory measurements of acoustic velocities at room temperature (Bass, 1995). Under natural conditions, elastic contrast (E_f/E_m) between garnet and quartz or feldspar may be larger than that in the laboratory. For comparison, we also calculate the tensile stress distribution in a lenticular particle using $E_f/E_m = 10$, $\nu = 0.08$ for quartz and $\nu = 0.30$ for feldspar, and the results are shown in Fig. 14. The following points can be highlighted.

(1) The tensile stress in a garnet grain is always larger than the far-field tensile stress applied on the composite rock (Figs 13 & 14) because the E value of garnet is larger than that of the felsic matrix. This is the reason why tensile fracturing takes place preferentially in garnet rather than in the surrounding felsic matrix. Since the maximum ratio σ_f/σ_m increases with E_f/E_m, it is not surprising that the maximum tensile stress in a garnet embedded in a quartz matrix is larger than that in a plagioclase matrix. Moreover, the maximum ratio σ_f/σ_m increases also with the garnet aspect ratio. Thus, grains which are aligned parallel to the direction of the applied stress and which have high aspect ratios break first. When one garnet crystal is broken during extension, the stress around it is relaxed, and the force carried by this crystal is transferred to the surrounding matrix and particularly neighboring garnet crystals.

(2) In an intact, lens-shaped stiff particle, the tensile stress is a maximum at the center and decays to σ_m at the apexes (Figs 13 & 14). Accordingly, the fracture will occur at the mid-point of the particle. Then, the entire lens is divided into two semi-lenses. The tensile stress distribution in the semi-lenses or in the truncated semi-lenses is asymmetrical with respect to their mid-point (Figs 13 & 14). The location of the maximum tensile stress is closer to the end with less cross-sectional area. If

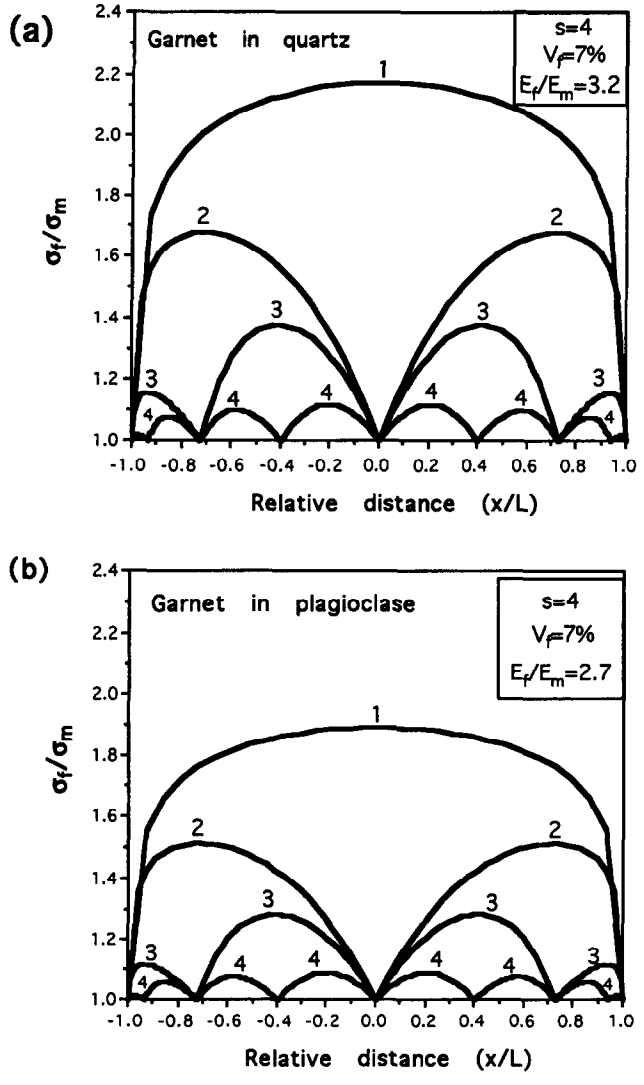

Fig. 13. Predicted tensile stress along each fragment produced by a sequential fracturing process of a lenticular garnet with an aspect ratio of 4. (a) Garnet in a quartz matrix, $E_f/E_m = 3.2$. (b) Garnet in a plagioclase matrix, $E_f/E_m = 2.7$. Elastic constants for quartz, plagioclase and garnet were taken from Bass (1995). The numbers infer fracture generations.

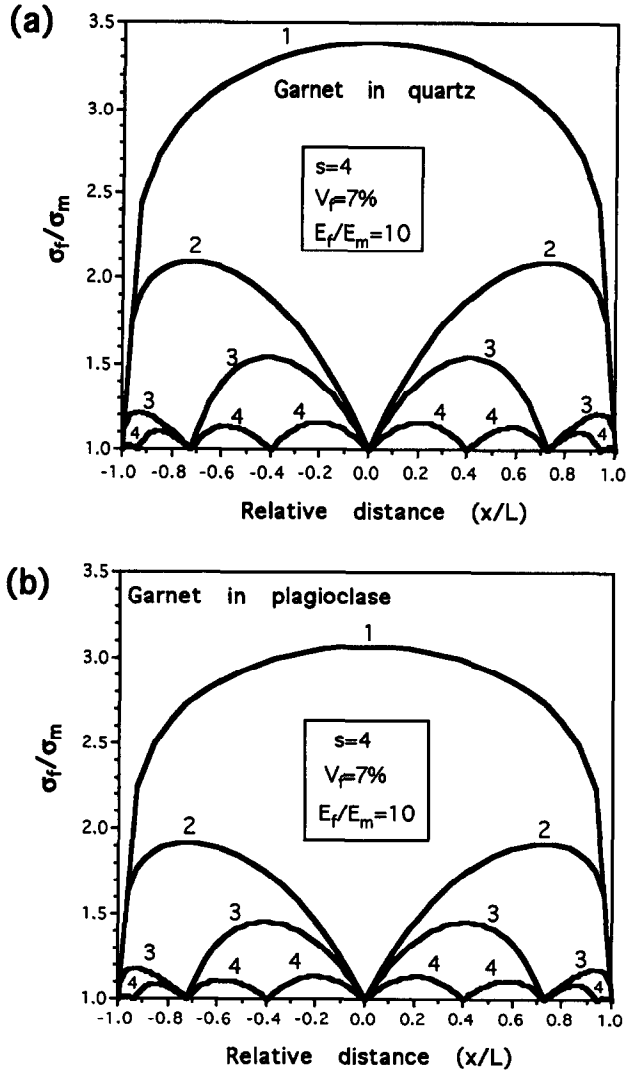

Fig. 14. Predicted tensile stress along each fragment produced by a sequential fracturing process of a lenticular garnet with an aspect ratio of 4. (a) Garnet in a quartz matrix with the Poisson ratio equal to 0.08. (b) Garnet in a plagioclase matrix with the Poisson ratio equal to 0.30. In both the cases, E_f/E_m are assumed to be equal to 10. The numbers infer fracture generations.

fracture occurs at the position of maximum tensile stress in a fractured segment of garnet, this segment will fragment into two sub-segments of unequal length, the longer of which has the larger diameter. We should point out that inhomogeneous distribution of microflaws may perturb the fracturing location predicted by the shear-lag model (Ferguson, 1987; Ji and Zhao, 1993).

(3) The fracturing process is sequential. After a breakage, the segments are newly loaded in the course of extension and break again. As each segment has one position of maximum tensile stress along the loading direction (Figs 13 & 14), the fractured garnet segment should never be broken along more than one plane at the same time provided the segment is mechanically homogeneous (Prior, 1993). As described before, a number of parallel tensile fractures occur in each single garnet grain. These fractures should belong to different generations which were formed by progressive uplift events. Each generation of fractures may correspond to a given thickness (e.g. 1 km) of unroofing. If the matrix were ductile, it could have flowed into the gaps between the segments (boudins). The temporal sequence of fracturing in a brittle inclusion in response to flow in the plastic matrix could thus be established according to different sized gaps between the boudins; larger gaps are associated with earlier fractures and smaller gaps with later fractures (Lloyd *et al.*, 1982; Masuda and Kuriyama, 1988; Ji and Zhao, 1993). In the present case, however, where both the matrix and the particle are elastic, fracture of the brittle particle in response to the elastic deformation in the surrounding matrix cannot be dilational although it is sequential. Hence, the time relationship of the fractures cannot be determined in a given garnet grain due to the lack of significant separation between the fractured segments.

(4) The magnitude of the tensile stress in a fractured segment of a given size decreases with decreasing length/diameter (aspect) ratio (Figs 13 & 14). The sequential fracturing process will decrease the aspect ratio and in consequence will reduce the tensile stress in the elastic–brittle segment. As shown in Fig. 7(d), aspect ratios of most fractured garnet segments are much smaller than 1 with an average value of only about 0.26. This means that, in the fracture direction (i.e. the direction normal to foliation), their aspect ratios have a mean value of 3.8. The tensile stress within the garnet increases in the direction normal to foliation so that fracture of garnet segments may become possible along a plane parallel to the foliation. Thus, two orthogonal fracture sets may occur in the same grain due to the above switch of aspect ratio for the fractured garnet segments (Fig. 15). In a plastic matrix, however, such a switch is almost impossible. Because the flow stress of the plastic matrix is much lower than the failure strength of the competent particle and because there may be slipping to some extent on the particle–matrix interface, the critical aspect ratio of fractured segments, below which the segments cannot undergo any further fracture, is generally larger than 0.5–1.0. Our interpretation of the ladder-like fracture sets may be applicable to orthogonal joint sets described by Nickelsen and Hough (1967) and Rawnsley *et al.* (1992). They interpreted the joints to be the result of residual stress relaxation during erosion and unloading.

It is interesting to compare the shear-lag model with the Eshelby model (Eshelby, 1957, 1959; see Mura, 1982 for a review). Both models predict an increase in internal stresses of a stiff inclusion as a result of strain misfit between this inclusion and the surrounding matrix. Unlike the shear-lag model, however, the Eshelby model predicts that the stresses inside an ellipsoidal inclusion are homogeneous. This conclusion is based on an assumption that the stresses applied to the infinite matrix surrounding the inclusion are homogeneous (Holzhausen and Johnson, 1979). As pointed out by Taya and Arsenault (1989), Eshelby's procedure to obtain the stress field outside the inclusion remains rigorous, but that for the stress field inside the inclusion is simplified. However, the shear-lag model assumes that the inclusion–matrix system is subjected to a longitudinal extension and the resulting lateral contraction. If the stresses inside garnets were homogeneous, we would expect a random distribution of the fracture spacing since pre-existing microflaws in an isotropic material like garnet are most likely to be randomly distributed (Lawn, 1993). Moreover, the results of the Eshelby model are applicable only to dilute composites in which the volume fraction of stiff inclusions is less than a few percent while those of the shear-lag model are applicable to both dilute and non-dilute systems (Clyne and Withers, 1993). In addition, the stresses in a non-ellipsoid-shaped inclusion (e.g. cylinder, lens or truncated ellipsoid) can be calculated much more easily using the shear-lag model than the Eshelby model.

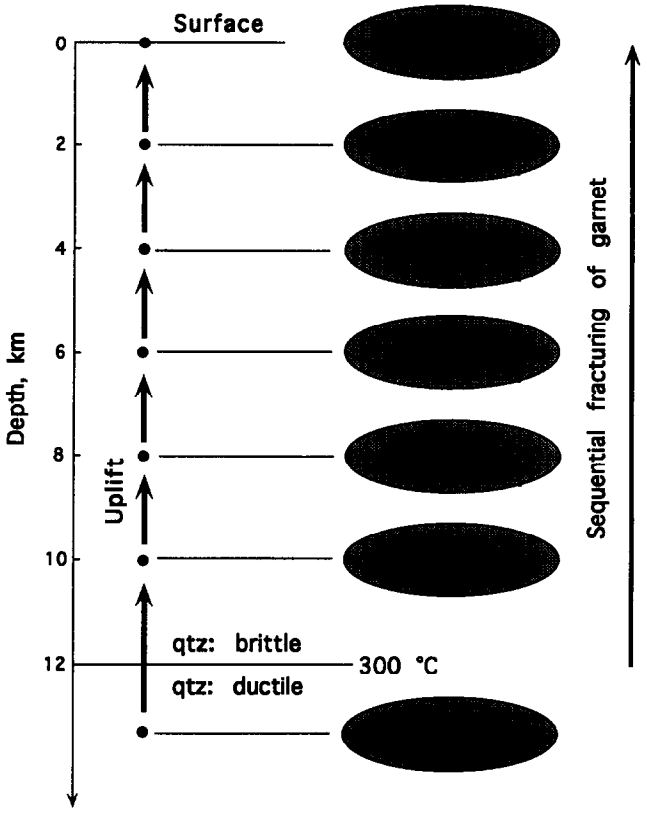

Fig. 15. Schematic illustration of two orthogonal sets of tensile fractures in a garnet. The earlier pervasive fractures are perpendicular to the lineation and the later less-pronounced fractures are parallel to the foliation (X–Y plane). Formation of these two set of tensile fractures are attributed to a decrease in the aspect ratio of garnet fragments due to the sequential fracturing process.

CONCLUSIONS

The results of this study are consistent with the following conclusions.

(1) Fractured garnets are an important feature of the well-foliated and lineated mylonites and gneisses from the granulite-facies Morin shear zone of the Grenville Province (Québec). They are clearly observed both in outcrop and in thin section. The pervasive, closely spaced, relatively straight fractures in garnet crystals are planar tensile fractures with no displacement parallel to the fracture plane. The fractures are preferentially perpendicular to the mylonitic foliation and lineation.

(2) The intragranular microfractures commonly taper from the grain boundary towards the core, suggesting that the fractures initiated at grain boundaries and then propagated inwards. This indicates that interfaces between different phases are mechanical and structural heterogeneities that control the initiation of fractures.

(3) The fractures developed preferentially in coarse

grains with a large aspect ratio. Fractures in grains smaller than 0.2 mm with an aspect ratio less than 2 are rare. This is probably because large grains contain more and larger microflaws than small grains (Lloyd, 1991) and because the stress transferred from the incompetent matrix to the competent particle increases with the particle aspect ratio.

(4) Regions of the rocks with clustered garnet crystals exhibit a greater degree of garnet fracture than regions where the local concentration of the garnet crystals is more dilute. This is because closely spaced strong particles cause a local stress concentration (Lloyd and Knipe, 1992).

(5) The fractured segments of each garnet crystal have not been separated or filled with matrix minerals such as quartz and feldspar or with retrogressive minerals such as biotite, muscovite and chlorite. Some garnet fractures extend into the surrounding quartz. Thus, the garnets were fractured at shallow crustal depths ($T < 300$°C, or < 15 km for a thermal gradient 20°C/km) where the mylonitic matrix was no longer capable of plastic flow at geologically reasonable strain rates.

(6) Laboratory measurements of P-wave velocities show that the mylonites and gneisses containing fractured garnets are elastically anisotropic; they are more compressible in the direction normal to the foliation than in the direction parallel to the lineation. Based on the measurement results, we suggest that the fractures in the garnet crystals formed by the response of anisotropic metamorphic rocks to horizontal extension during uplift and cooling of the metamorphic terrane within the upper crust.

(7) Based on the fundamental assumptions of the shear-lag theory of Cox (1952) and Kelly and Macmillan (1986), we develop a new mechanical model for a particle–matrix system. The particle is assumed to be a rotational body with any given longitudinal section (e.g. lens, ellipsoid, truncated ellipsoid). This new model explains well why tensile fracturing took place preferentially in stiff garnet rather than in incompetent felsic material, why two sets of tensile fractures could form in the same garnet grains, and why the fractures are unequally spaced in a lenticular or ellipsoidal garnet grain.

(8) Our results suggest that the sequential tensile fractures of garnet grains record a progressive uplift process of metamorphic rocks within the upper crust.

Acknowledgements—This study was supported by grants from the NSERC of Canada and the FCAR of Quebec to S. Ji. We thank S. Hanmer, P.-Y. Robin and P. F. Williams for helpful discussion during a Canadian Tectonic Group field trip in the study area guided by J. Martignole and S. Ji. S. Hanmer, J. Martignole and B. Lafrance are thanked for critical reading an early version of this manuscript. Dr R. J. Norris, Dr D. J. Prior and an anonymous reviewer are thanked for their critical reviews of the paper. LITHOPROBE Contribution No. 847.

REFERENCES

Bass, J. D. (1995) Elasticity of minerals, glasses, and melts. In *Mineral Physics and Crystallography: A Handbook of Physical Constants*, ed. T. J. Ahrens, pp. 45–63. American Geophysical Union, Washington, DC.

Birch, F. (1960) The velocity of compressional waves in rocks to 10 kilobars, Part 1. *Journal of Geophysical Research* **65**, 1083–1102.

Bruner, W. M. (1984) Crack growth during unroofing of crustal rocks: effects on thermoelastic behavior and near-surface stresses. *Journal of Geophysical Research* **89**, 4167–4184.

Chopin, C. (1984) Coesite and pure pyrope in high-grade blueschists of the western Alps: a first record and some consequences. *Contributions to Mineralogy and Petrology* **86**, 107–118.

Christensen, N. I. and Shaw, G. (1970) Elasticity of mafic rocks from the middle-Atlantic Ridge. *Geophysics Journal* **20**, 271–284.

Cleveland, J. J. and Bradt, R. C. (1978) Grain size/microcracking relations for pseudobrookite oxides. *Journal of the American Ceramics Society* **61**, 478–481.

Clyne, T. W. and Withers, P. J. (1993) *An Introduction to Metal Matrix Composites*. Cambridge University Press, New York.

Cox, H. L. (1952) The elasticity and strength of paper and other fibrous materials. *British Journal of Applied Physics* **3**, 72–79.

Doig, R. (1991) U–Pb zircon dates of Morin anorthosite suite rocks, Grenville Province, Quebec. *Journal of Geology* **99**, 729–738.

Drucker, D. C. (1965) Engineering and continuum aspects of high-strength materials. In *High Strength Materials*, ed. V. Zackay, pp. 795–833. Wiley, New York.

Dunand, D. C. and Mortensen, A. (1991) Dislocation emission at fibers I. Theory of longitudinal punching by thermal stresses. *Acta Metallurgica et Materialia* **39**, 1405–1416.

Elvevold, S., Reginiussen, H., Krogh, E. J. and Bjorklund, F. (1994) Reworking of deep-seated gabbros and associated contact metamorphosed paragneisses in the south-eastern part of the Seiland Igneous Province, Northern Norway. *Journal of Metamorphic Geology* **12**, 539–556.

Eshelby, J. D. (1957) The determination of the elastic field of an ellipsoidal inclusion, and related problems. *Proceedings of the Royal Society of London* **A241**, 376–396.

Eshelby, J. D. (1959) The elastic field outside an ellipsoidal inclusion. *Proceedings of the Royal Society of London* **A252**, 561–569.

Evans, A. G. (1978) Microfracture from thermal expansion anisotropy I. Single phase systems. *Acta Metallurgica* **26**, 1845–1853.

Fei, Y. (1995) Thermal expansion. In *Mineral Physics and Crystallography: a Handbook of Physical Constants*, ed. T. J. Ahrens, pp. 29–44. American Geophysical Union, Washington, DC.

Ferguson, C. C. (1987) Fracture and separation histories of stretched belemnites and other rigid–brittle inclusions in tectonites. *Tectonophysics* **139**, 255–273.

Fredrich, J. T. and Wong, T. (1986) Micromechanics of thermally induced cracking in three crustal rocks. *Journal of Geophysical Research* **91**, 12743–12764.

Gillet, P., Ingrin, J. and Chopin, C. (1984) Coesite in subducted continental crust: P–T history deduced from an elastic model. *Earth and Planetary Science Letters* **70**, 426–436.

Gross, M. R. (1993) The origin and spacing of cross joints: examples from the Monterey Formation, Santa Barbara Coastline, California. *Journal of Structural Geology* **15**, 737–751.

Haxby, W. F. and Turcotte, D. L. (1976) Stresses induced by the addition or removal of overburden and associated thermal effects. *Geology* **4**, 181–184.

Hippertt, J. F. M. (1993) 'V'-pull-apart microstructures: a new shear sense indicator. *Journal of Structural Geology* **15**, 1393–1403.

Holister, G. S. and Thomas, C. (1966) *Fiber Reinforced Materials*. Elsevier, New York.

Holzhausen, G. R. and Johnson, A. M. (1979) The concept of residual stress in rock. *Tectonophysics* **58**, 237–267.

Indares, A. (1995) Metamorphic interpretation of high-pressure–temperature metapelites with preserved growth zoning in garnet, eastern Grenville Province, Canadian Shield. *Journal of Metamorphic Geology* **13**, 475–486.

Ji, S. and Martignole, J. (1994) Ductility of garnet as an indicator of extremely high temperature deformation. *Journal of Structural Geology* **16**, 985–996.

Ji, S. and Martignole, J. (1996) Ductility of garnet as an indicator of extremely high temperature deformation: Reply. *Journal of Structural Geology* **18**, 1375–1380.

Ji, S., Salisbury, M. H. and Hanmer, S. (1993) Petrofabric, P-wave anisotropy and seismic reflectivity of high-grade tectonites. *Tectonophysics* **222**, 195–226.

Ji, S. and Zhao, P. (1993) Location of tensile fracture within rigid–brittle inclusions in ductilely flowing matrix. *Tectonophysics* **220**, 23–31.

Ji, S. and Zhao, P. (1994) Strength of two-phase rocks: a model based on fiber-loading theory. *Journal of Structural Geology* **16**, 253–262.

Kelly, A. and Macmillan, N. H. (1986) *Strong Solids*. Oxford Science Publications, London.

Kelly, A. and Street, K. N. (1972) Creep of discontinuous fibre composites: II. Theory for the steady-state. *Proceedings of the Royal Society of London* **A328**, 283–293.

Ladeira, F. L. and Price, N. J. (1981) Relationship between fracture spacing and bed thickness. *Journal of Structural Geology* **3**, 179–183.

Lawn, B. (1993) *Fracture of Brittle Solids*. Cambridge University Press, Cambridge.

Lee, J. K. W. and Tromp, J. (1995) Self-induced fracture generation in zircon. *Journal of Geophysical Research* **100**, 17753–17770.

Li, C. and Ellyin, F. (1995) Short crack growth behavior in a particulate-reinforced aluminum alloy composite. *Metallurgical and Materials Transactions* **A26**, 3177–3182.

Lloyd, D. (1991) Aspects of particle fracture in particulate reinforced MMCs. *Acta Metallurgica et Materialia* **39**, 59–72.

Lloyd, G. E., Ferguson, C. C. and Reading, K. (1982) A stress-transfer model for the development of extension fracture boudinage. *Journal of Structural Geology* **4**, 355–372.

Lloyd, G. E. and Knipe, R. J. (1992) Deformation mechanisms accommodating faulting of quartzite under upper crustal conditions. *Journal of Structural Geology* **14**, 127–143.

Martignole, J. (1975) Le Précambrien dans le sud de la Province tectonique de Grenville. Doctorat d'Etat thesis, Université de Toulouse.

Martignole, J., Ji, S. and Zhao, X. (1995) *High Temperature Mylonites of the Morin Shear Zone (Grenville Province, Quebec)*. Canadian Tectonic Group Meeting, Field Guide.

Martignole, J. and Schrijver, K. (1970) Tectonic setting and evolution of the Morin Anorthosite, Grenville Province, Quebec. *Bulletin of the Geological Society of Finland* **42**, 165–209.

Masuda, T. and Kuriyama, M. (1988) Successive 'mid-point' fracturing during microboudinage: an estimate of the stress–strain relation during a natural deformation. *Tectonophysics* **147**, 171–177.

McLean, D. (1972) Viscous flow of aligned composites. *Journal of Materials Science* **7**, 98–104.

Michibayashi, K. (1996) The role of intragranular fracturing on grain size reduction in feldspar during mylonitization. *Journal of Structural Geology* **18**, 17–25.

Moecher, D. P. and Wintsch, R. P. (1994) Deformation-induced reconstitution and local resetting of mineral equilibrium in polymetamorphic gneisses: tectonic and metamorphic implications. *Journal of Metamorphic Geology* **12**, 523–538.

Mura, T. (1982) *Micromechanics of Defects in Solids*. Martinus Nijhoff, Boston.

Nardone, V. C. and Prewo, K. M. (1986) On the strength of discontinuous silicon carbide reinforced aluminum composites. *Scripta Metallurgica et Materialia* **20**, 43–48.

Nichols, T. C. (1980) Rebound, its nature and effect on engineering works. *Quarterly Journal of Engineering Geology* **13**, 133–152.

Nickelsen, R. P. and Hough, V. N. D. (1967) Jointing in the Appalachian plateau of Pennsylvania. *Bulletin of the Geological Society of America* **78**, 609–629.

Petrakakis, K. (1986) Metamorphism of high-grade gneisses from the Moldanubian zone, Austria, with particular reference to the garnets. *Journal of Metamorphic Geology* **4**, 323–344.

Price, N. J. and Cosgrove, J. W. (1990) *Analysis of Geological Structures*. Cambridge University Press, Cambridge.

Prior, D. J. (1993) Sub-critical fracture and associated retrogression of garnet during mylonitic deformation. *Contributions to Mineralogy and Petrology* **113**, 545–556.

Prior, D. J. and Behrmann, J. H. (1990) Thrust-related mudstone fabrics from the Barbados forearc: A backscattered scanning electron microscope study. *Journal of Geophysical Research* **95**, 9055–9067.

Rawnsley, K. D., Rives, T., Petit, J.-P., Hencher, S. R. and Lumsden, A. C. (1992) Joint development in perturbed stress fields near faults. *Journal of Structural Geology* **14**, 939–951.

Reynolds, S. J. and Lister, G. S. (1987) Structural aspects of fluid–rock interactions in detachment zones. *Geology* **15**, 362–366.

Rice, R. W. and Pohanka, R. C. (1979) Grain-size dependence of spontaneous cracking in ceramics. *Journal of the American Ceramics Society* **62**, 559–563.

Rivers, T., Martignole, J., Gower, C. F. and Davidson, A. (1989) New tectonic divisions of the Grenville Province. *Tectonics* **8**, 63–84.

Scholz, C. H. (1990) *The Mechanics of Earthquakes and Faulting*. Cambridge University Press, New York.

Suppe, J. (1985) *Principles of Structural Geology*. Prentice-Hall, Englewood Cliffs, New Jersey.

Turcotte, D. L. and Schubert, G. (1982) *Geodynamics*. Wiley, New York.

Tvergaard, V. and Hutchinson, J. W. (1988) Microcracking in ceramics induced by thermal expansion or elastic anisotropy. *Journal of the American Ceramics Society* **71**, 157–166.

Taya, M. and Arsenault, R. J. (1989) *Metal Matrix Composites*. Pergamon Press, New York.

Valentino, A. J. and Sclar, C. B. (1981) Parting in giant garnets as an indicator of late brittle deformation at Gore Mountain, Warren County, N.Y. *Geophysical Research Letters* **8**, 883–885.

van der Molen, I. (1981) The shift of the α–β transition temperature of quartz associated with the thermal expansion of granite at high pressure. *Tectonophysics* **73**, 323–342.

Watt, D. F., Xu, X. Q. and Lloyd, D. J. (1996) Effects of particle morphology and spacing on the strain fields in a plastically deforming matrix. *Acta Materialia* **44**, 789–799.

Wendt, A. S., D'Arco, P., Goffe, B. and Oberhansli, R. (1993) Radial cracks around α-quartz inclusions in almandine: constraints on the metamorphic history if the Oman mountains. *Earth and Planetary Science Letters* **114**, 449–461.

Whitney, D. L. (1996) Garnets as open systems during regional metamorphism. *Geology* **24**, 147–150.

Yardley, B. W. D. (1977) An empirical study of diffusion in garnet. *American Mineralogy* **62**, 793–800.

Zhang, R., Hirajima, T., Banno, S., Cong, B. and Liou, J. G. (1995) Petrology of ultrahigh-pressure rocks from the southern Su-Lu region, eastern China. *Journal of Metamorphic Geology* **13**, 659–675.

APPENDIX

Mechanical model for an inclusion–matrix system

We consider a basic unit cell consisting of a stiff inclusion embedded completely in a continuous incompetent matrix (Fig. A1a). This inclusion is represented by a rotation body with any given longitudinal section (lens, ellipsoid or truncated ellipsoid). Both the inclusion and the matrix deform elastically. The inclusion has a long axis length of $2L$ and short axis length of $2r_0$. The rotation axis or the long axis is parallel to the x-axis (Fig. A1a). In order to obtain the relationship between the longitudinal stress in the inclusion and the far-field stress in the matrix, we will deal with the equilibrium of an infinitesimal element shown in Fig. A1(b). Because the total axial force along the x-direction should be equal to zero under the equilibrium conditions, we have

$$\begin{aligned}&\pi[r_0(x)+\mathrm{d}r_0(x)]^2[\sigma(x)+\mathrm{d}\sigma(x)]-\pi[r_0(x)]^2\sigma(x)\\&+2\pi r_0(x)\tau_0(x)\mathrm{d}x+2\pi[r_0(x)+\mathrm{d}r_0(x)]\sigma_m\mathrm{d}x\tan\theta=0\quad(x\geq 0)\end{aligned}\tag{A1}$$

and

$$\begin{aligned}&\pi[r_0(x)+\mathrm{d}r_0(x)]^2[\sigma(x)+\mathrm{d}\sigma(x)]-\pi[r_0(x)]^2\sigma(x)+2\pi r_0(x)\tau_0(x)\mathrm{d}x\\&-2\pi[r_0(x)+\mathrm{d}r_0(x)]\sigma_m\mathrm{d}x\tan\theta=0\quad(x<0),\end{aligned}\tag{A2}$$

where $r_0(x)$ is the radius of the circular cross-section of the inclusion at x, $\sigma(x)$ is the axial tensile stress on the circular cross-section with a radius of $r_0(x)$, σ_m is the far-field stress in the matrix and θ is the angle between the x-axis and the tangent of the rotational surface at x. All the terms in equations (A1) and (A2) are also defined in Fig. A1.

In the infinitesimal element shown in Fig. A1(b),

$$\tan\theta=\begin{cases}-\dfrac{\mathrm{d}r_0(x)}{\mathrm{d}x} & (x\geq 0)\\[2ex] \dfrac{\mathrm{d}r_0(x)}{\mathrm{d}x} & (x<0).\end{cases}\tag{A3}$$

Ignoring the high-order differential terms and considering equation (A3), equations (A1) and (A2) can be combined and rewritten as

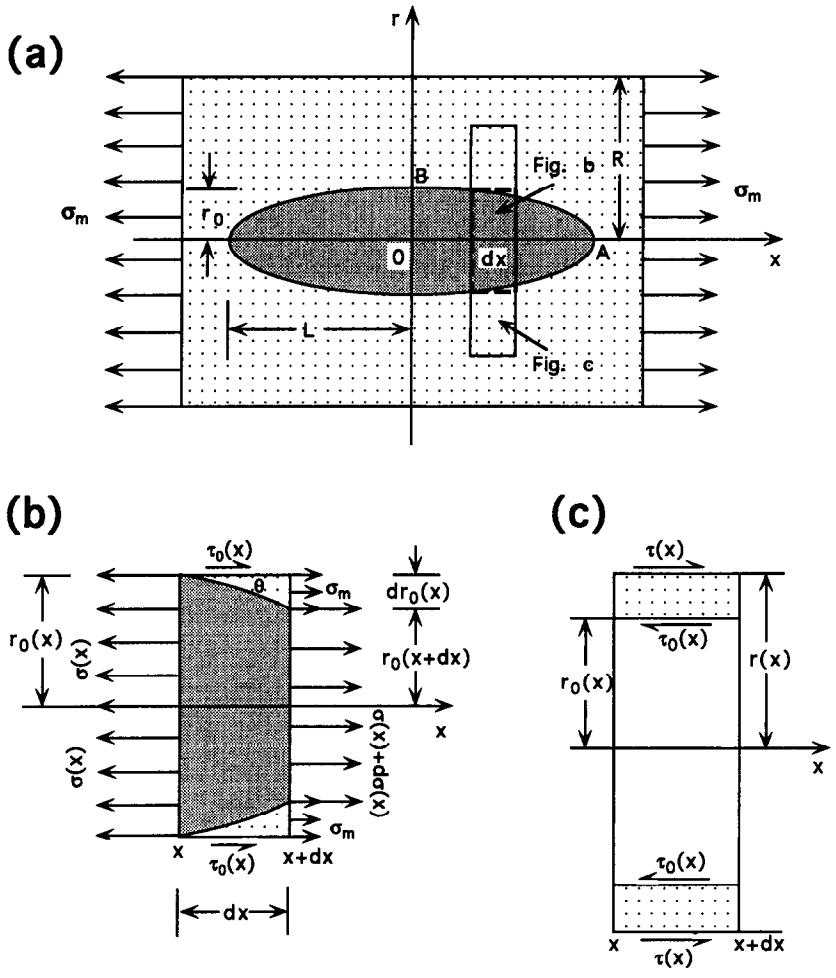

Fig. A1. Schematic illustration of the mechanical equilibrium analysis in the shear-lag model. (a) Unit cell containing a stiff rotational body (e.g. ellipsoidal inclusion) embedded completely in an incompetent matrix. (b) Infinitesimal element of the inclusion. (c) Internal stress distribution in the matrix surrounding the infinitesimal element of the inclusion.

$$r_0(x)^2\frac{d\sigma(x)}{dx}+2r_0(x)\sigma(x)\frac{dr_0(x)}{dx}+2r_0(x)\tau_0(x)-2\sigma_m r_0(x)\frac{dr_0(x)}{dx}=0. \tag{A4}$$

According to the shear-lag model (Cox, 1952; Kelly and Macmillan, 1986), the shear stress, $\tau(r,x)$, on the circular ring surface in the matrix around the inclusion (Fig. A1c) is proportional to the difference between the longitudinal displacement u in the matrix close to the inclusion and the displacement of the matrix (v) at the same point if the inclusion were absent, that is,

$$-2\pi r(x)\tau(r,x)=H(u-v). \tag{A5}$$

If there is no slip at the inclusion–matrix interface (Cox, 1952; Kelly and Macmillan, 1986), then we have $u=w$, where w is the longitudinal displacement in the inclusion, when $r(x)=r_0(x)$,

$$-2\pi r_0(x)\tau_0(x)=H(w-v). \tag{A6}$$

At a distance from the x-axis of the inclusion equal to half the average spacing (R) between inclusions, we have $u=v$. The R value depends on the volume fraction (V_f), shape and size of the inclusion and the length of the unit cell. If we consider the equilibrium of the matrix between r_0 and $r(x)$ ($r_0\le r(x)\le R$) (Fig. A1c), we have

$$2\pi r(x)\tau(r,x)=2\pi r_0(x)\tau_0(x) \tag{A7}$$

and so the shear strain in the matrix is given by the following equation:

$$\frac{\partial u}{\partial r}=\frac{\tau(r,x)}{G_m}=\frac{\tau_0(x)r_0(x)}{G_m r(x)}, \tag{A8}$$

where G_m is the shear modulus of the matrix. Integrating equation (A8) from r_0 to R,

$$\Delta u=\frac{\tau_0(x)r_0(x)}{G_m}\ln\left(\frac{R(x)}{r_0(x)}\right). \tag{A9}$$

Because $\Delta u=v-w$, using equations (A6) and (A9), we have

$$H(x)=\frac{2\pi G_m}{\ln\left(\dfrac{R}{r_0(x)}\right)}. \tag{A10}$$

Substituting equation (A6) into equation (A4), we obtain

$$r_0(x)^2\frac{d\sigma(x)}{dx}+2r_0(x)\sigma(x)\frac{dr_0(x)}{dx}-\frac{H}{\pi}(w-v)-2\sigma_m r_0(x)\frac{dr_0(x)}{dx}=0. \tag{A11}$$

Differentiating equation (A11) and considering

$$\varepsilon=\frac{dv}{dx} \tag{A12}$$

and

$$\frac{dw}{dx}=\frac{\sigma(x)}{E_f} \tag{A13}$$

we can obtain the final differential equation for the tensile stress as a function of distance along the x-direction in the inclusion:

$$\frac{d^2\sigma(x)}{dx^2}+A(x)\frac{d\sigma(x)}{dx}+B(x)\sigma(x)=C(x), \tag{A14}$$

where

$$A(x) = \frac{4}{r_0(x)}\frac{\mathrm{d}r_0(x)}{\mathrm{d}x} - \frac{1}{H(x)}\frac{\mathrm{d}H(x)}{\mathrm{d}x} \tag{A15}$$

$$B(x) = \frac{2}{r_0(x)^2}\left(\left(\frac{\mathrm{d}r_0(x)}{\mathrm{d}x}\right)^2 + r_0(x)\left(\frac{\mathrm{d}^2 r_0(x)}{\mathrm{d}x^2}\right) - \frac{r_0(x)}{H(x)}\frac{\mathrm{d}H(x)}{\mathrm{d}x}\frac{\mathrm{d}r_0(x)}{\mathrm{d}x} - \frac{H(x)}{2\pi E_\mathrm{f}}\right) \tag{A16}$$

and

$$C(x) = \frac{2E_\mathrm{m}\varepsilon}{r_0(x)^2}\left(\left(\frac{\mathrm{d}r_0(x)}{\mathrm{d}x}\right)^2 + r_0(x)\left(\frac{\mathrm{d}^2 r_0(x)}{\mathrm{d}x^2}\right) - \frac{r_0(x)}{H(x)}\frac{\mathrm{d}H(x)}{\mathrm{d}x}\frac{\mathrm{d}r_0(x)}{\mathrm{d}x}\right) - \frac{H(\varepsilon)}{\pi r_0(x)^2}. \tag{A17}$$